Correcting for salt misinterpretation with full-waveform inversion

Zhigang Zhang, Jiawei Mei, Feng Lin, Rongxin Huang, and Ping Wang (CGG)*

Summary

Using full-waveform inversion (FWI) to update velocity models that contain salt bodies with high velocity contrasts is challenging. It is even harder if erroneous salt geometry is part of the velocity model. Shen et al. (2017) showed a successful FWI application that corrected some misinterpretation of salt structures and resulted in improved subsalt images at the Atlantis field in the Gulf of Mexico. Their study stressed the importance of the low frequencies (usable down to 1.6 Hz), full azimuths, and long offsets of OBN data. Encouraged by the success at Atlantis, we revisited some aspects of FWI algorithms to minimize cycle-skipping and amplitude discrepancy issues that are common in the presence of salt and salt misinterpretation. Here we present the use of traveltime misfit measured in frequency-dependent time windows as the FWI cost function. It is devised to minimize the negative impact from the amplitude discrepancy and cycle-skipping between the recorded data and modeled synthetic data. Furthermore, we use the crosscorrelation coefficient between the recorded data and synthetic data as a weight function in gradient computation to promote traveltime measurements of higher quality. We demonstrate the effect of our approach using a full-azimuth streamer data set in an area of complex shallow salt bodies in the Gulf of Mexico.

Introduction

Among other factors, one key for subsalt imaging is to build the salt velocity model. Current standard practice for salt model building is to use tomography, sometimes combined with shallow diving-wave full-waveform inversion (FWI), to first build the best possible sediment velocity model. Then, a sediment-flood migration is used for top-of-salt (TOS) interpretation, followed by a salt-flood migration for base-of-salt (BOS) interpretation. In the next step, a number of salt scenario tests are usually required to resolve the salt geometry, especially for complex areas. This procedure is not only labor-intensive and time-consuming, but it is also prone to human misinterpretation. FWI is considered the most promising data-driven tool to automatically build velocity models by iteratively minimizing the difference between recorded data and modeled synthetic data (Tarantola, 1984). Many successful examples have been reported using FWI to update shallow sediments, gas pockets, and mud volcanoes. However, the success of using FWI to update salt structures remained missing until the recent progress at the Atlantis field, Gulf of Mexico (GoM) using low-frequency, full-azimuth, and long-offset OBN data (Michell et al., 2017; Shen et al., 2017).

Two major issues that cause FWI to fail are cycle-skipping and amplitude discrepancy between synthetic data and recorded data, particularly when there are sharp contrasts and large-scale geobodies (e.g., salt bodies) in the model. When phases, or traveltime differences, between synthetic and recorded data are large, the oscillatory pattern of the seismic signals introduces local minima. FWI may attempt to fit the synthetic data to a wrong cycle in the recorded data. Additionally, the amplitude distribution of recorded seismic data is usually very different from that of synthetics. If this difference is not appropriately addressed, it will be interpreted as velocity error by FWI, which leads the inversion to erroneous velocity models.

Many methods to solve the issues of cycle-skipping and amplitude discrepancy have been proposed (Luo and Schuster, 1991; Ma and Hale, 2013). The traveltime difference of seismic signals is more linearly related to the velocity error than the waveform difference and any discrepancies in the amplitude difference are inconsequential. Alternatively, synthetic and recorded data can be brought in phase by applying a matching filter to one of the two data sets (Warner and Guasch, 2014).

Our proposed FWI workflow adopts the traveltime cost function proposed by Luo and Schuster (1991) with a frequency-dependent time window for traveltime measurements and a crosscorrelation coefficient-based weight function to promote traveltime measurements with high quality. Next, we explain our workflow in detail and demonstrate that this workflow is able to update the salt geometry, and thus significantly improve TOS/BOS and subsalt imaging, using a full-azimuth streamer data set in Keathley Canyon, GoM.

Method

FWI minimizes the difference between synthetic and recorded data (Lailly, 1983; Tarantola, 1984):

$$\chi(m) = \sum_{s,r}[d(t) - u(t,m)]^2, \quad (1)$$

where χ denotes the cost function, d is the recorded data, u is the synthetic data, m is the velocity model, t is the time, and s and r are the source and receiver index, respectively.

Compared to the least-squares cost function in Equation 1, a traveltime misfit function is more linear with respect to the difference between initial and true velocity models (Luo and Schuster, 1991). It reduces the nonlinearity of the inversion and mitigates the cycle-skipping issue. Moreover, in practice, an acoustic modeling engine is often used to simulate the seismic wave propagation process. As a result, there are elastic effects that are not properly modeled. Combined with uncertainties in the density model, it is

10.1190/segam2018-2997711.1

nearly impossible to generate synthetic data with amplitudes matching the real data. The cost function using traveltime measurements discards the amplitude differences. Consequently, it limits the amplitude impact when combined with the acoustic modeling engine.

The key to a traveltime-based FWI cost function is the measurement of the traveltime between the recorded data and modeled synthetic data. The traveltime difference is often obtained by maximizing the crosscorrelation of synthetic (u) and real data (d) in a time window between t_1 and t_2:

$$\Delta\tau = \text{argmax}_\tau \int_{t_1}^{t_2} d(t+\tau)u(t)dt. \quad (2)$$

One challenge for traveltime measurements is to determine the optimal window size. From one aspect, a short time window ($t_2 - t_1$) is required to capture the nonstationary variations of the traveltime for different events. From another aspect, a longer time window is preferred when there is strong noise in the input data. We found that a frequency-dependent time-window scheme is a good fit-for-purpose solution: at low frequencies, where the wavelet is longer and the data is often noisier, it makes sense to use a longer time window; as it goes to higher frequencies, where the wavelet becomes shorter and the data becomes cleaner (also, the velocity error is hopefully smaller as well due to low-frequency FWI update), a shorter time window can be used to measure the traveltime more precisely. Another challenge is that the measurements can be inaccurate due to strong noise and/or large differences between the recorded data and synthetic data. To reduce the negative impact from poor traveltime measurements or to promote high-quality traveltime measurements, we can use the crosscorrelation coefficients between the recorded data (shifted by the traveltime measurement) and synthetic data as a weight to encourage more reliable measurements to drive the inversion:

$$c(\Delta\tau) = \frac{\int_{t_1}^{t_2} d(t+\Delta\tau)u(t)dt}{\sqrt{\int_{t_1}^{t_2} d(t+\Delta\tau)d(t+\Delta\tau)dt}\sqrt{\int_{t_1}^{t_2} u(t)u(t)dt}}. \quad (3)$$

After obtaining the traveltime measurements and the weight function, we can formulate our FWI cost function as follows:

$$\chi(m) = \sum_{s,r,w} c\Delta\tau^2, \quad (4)$$

where w is the window index. The gradient can then be constructed by the adjoint-state method. The adjoint source of the proposed cost function is given by

$$\sum_{s,r,w} c(\Delta\tau)\Delta\tau \frac{\partial}{\partial t} d(t+\Delta\tau). \quad (5)$$

Field data examples

The study area is located in Keathley Canyon, in the central GoM, which is to the interior of the Sigsbee Escarpment and features complex salt structures (Figure 1a, blue box). The data was acquired using multiple vessels in a staggered configuration (Figure 1b). The five circles represent the source boats, the blue lines stand for the leading receiver boat, and the red lines are for the tailing receiver boat. The towed streamers had variable depths ranging between 10 m and 50 m (Mandroux et al., 2013). The rose diagram in Figure 1c shows that this acquisition configuration provided full-azimuth coverage up to 10 km and ultra-long offsets up to 18 km. Figure 2 shows the time-domain and phase-domain QC of this data. We can see that there are apparent signals down to 2.5 Hz, thanks to the deep tow depth of the streamers down to 50 m, compared to ~4 Hz for a typical shallow-towed streamer data set.

Since our new FWI method is still mostly driven by diving-wave energy, we deliberately identified a testing area where the salt body is at a shallow depth of 4-5 km and thus well sampled by the diving waves of this data set. The initial velocity model to our new FWI workflow is a smoothed version of the legacy model that was obtained after several iterations of ray-based reflection tomography and our previous diving-wave FWI for the overburden, followed by typical salt interpretation and subsalt velocity updates. Similarly to most other FWI approaches, we first determined the lowest starting frequency. Based on the QC in Figure 2 and our past experience with previous FWI approaches, we would typically choose a starting frequency of 3.5 Hz since the S/N at 2.5 Hz appears very low. To our surprise, we obtained better results with our new FWI workflow when we used a starting frequency of 2.5 Hz instead of 3.5 Hz. This indicates that our new FWI workflow has good tolerance for low-frequency noise because of the frequency-dependent time-window traveltime cost function and the crosscorrelation coefficient-based weight function.

Figures 3a and 3b show an inline section with velocity overlaid on the reverse-time migration (RTM) stack image for the initial model (a smoothed version of the legacy model) and the FWI-updated model (straight output with minimal editing to mute off updates below 6 km which are not well sampled by diving-wave energy), respectively. As expected, the velocity update from our new FWI flow is very small in the shallow sediment. There are some detailed changes around the TOS, especially at the salt finger marked by the white circle, and the salt geometry is slightly reshaped. The salt geometry changes were more noticeable on the depth slice at ~3 km (Figures 3c-d). We note that, although slightly sharper than in the initial model, the salt boundary after FWI is smooth overall compared to the typical salt models built with a standard velocity-model building (VMB) flow. This is partly because we used an initial model with smooth salt to begin with and only ran FWI up to 6.3 Hz. We expect to see sharper salt boundaries as it goes to higher FWI frequencies. Figure 4 shows the RTM stack image comparison between the initial model (a

10.1190/segam2018-2997711.1

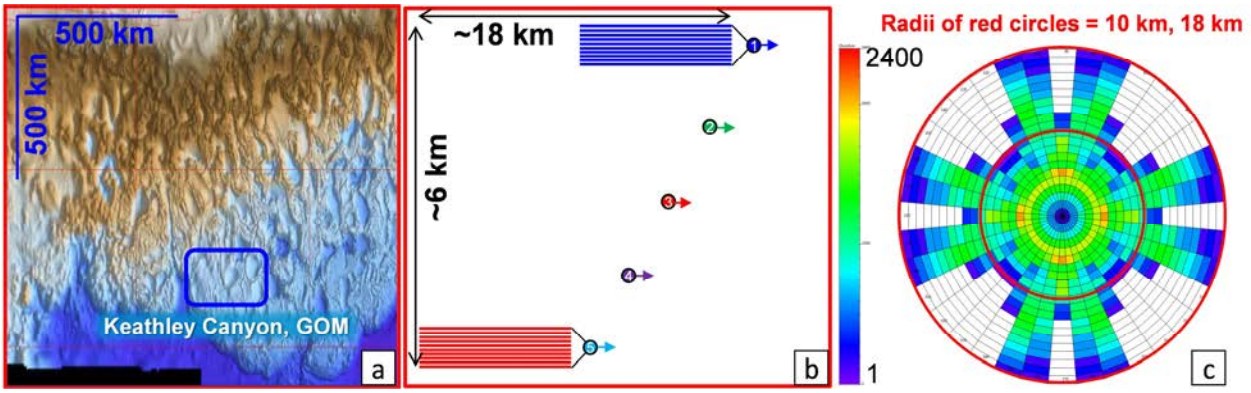

Figure 1: (a) Bathymetry in Keathley Canyon, Gulf of Mexico. (b) Staggered receiver acquisition geometry. (c) Rose diagram considering reciprocity. The inner circle marks 10 km offset, and the outer circle represents 18 km offset. The color bar represents the fold.

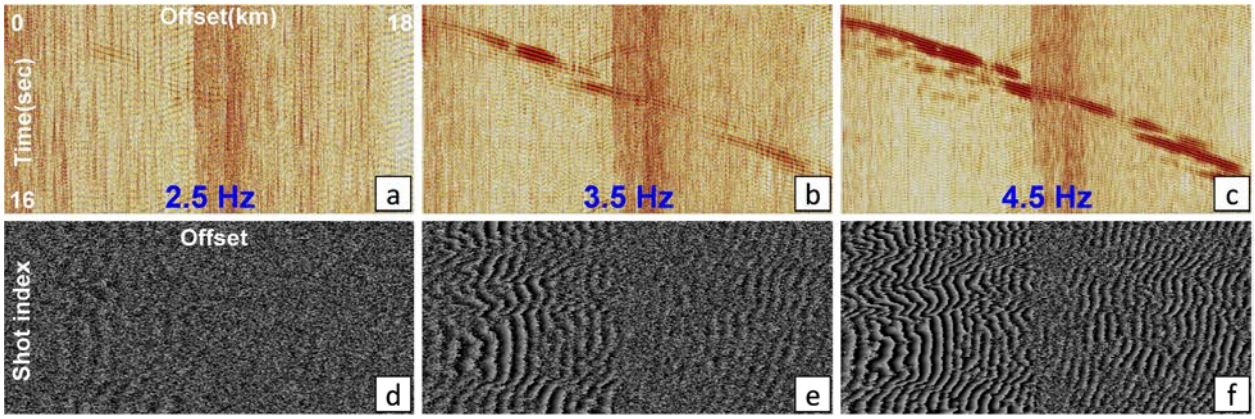

Figure 2: Time-domain QC at (a) 2.5 Hz, (b) 3.5 Hz, and (c) 4.5 Hz for one shot gather, which was from Gun #1 (dark blue circle in Figure 1b) with receivers on one cable from the leading boat (blue lines in Figure 1b) and another cable from the tailing boat (red lines in Figure 1b); and phase-domain QC at (d) 2.5 Hz, (e) 3.5 Hz, and (f) 4.5 Hz for the same gun-cable pair with all the shots from one sequence.

smoothed version of the legacy model) and the FWI-updated model (straight output with minimal editing to mute off the updates below 6 km which are not well sampled by diving-wave energy). Figures 4a-b show the comparison in a shallow window from 2-5 km. We observed that the salt finger is poorly imaged with the initial model, whereas it is well imaged with a clearly defined overhang boundary after FWI (see the dashed line in Figure 4b). Both the TOS and BOS are better imaged using the FWI model as well (arrows in Figure 4b). Figures 4c-d show the comparison in a deep window from 6-10 km. The image uplift after FWI is obvious at a depth as deep as 10 km (circle in Figure 4d). Not shown here, we also compared the FWI results with those using the legacy model without any smoothing, and all the conclusions remained the same.

Discussion and conclusions

We presented an FWI workflow that uses a frequency-dependent time-window traveltime cost function to mitigate the cycle-skipping and amplitude-discrepancy issues between synthetic data and recorded seismic data and that uses a crosscorrelation coefficient-based weight function to promote traveltime measurements with high quality. The field data example shows that with well-acquired data and the right geologic setting, our proposed approach is capable of updating salt geometry and thus improving TOS and BOS imaging, as well as subsalt imaging down to 10 km. We would like to point out that the velocity updates for this example are subtle overall, but their impact on the image is not small. These subtle changes are very hard to resolve by our standard VMB flow.

We note that our FWI approach is still mostly driven by diving-wave energy, though reflection data were also found to be useful but only if the diving-wave energy is adequate for FWI to provide a good enough low-wavenumber background velocity model. Low-frequency, long-offset, and full-azimuth data is still required to update complex salt structures with not-so-small velocity errors. In the example presented here, the data set has full azimuth

10.1190/segam2018-2997711.1

coverage up to 10 km and long offsets up to 18 km with usable frequencies down to 2.5 Hz, which is a much better data set than most existing towed-streamer data sets. Furthermore, the salt body in this area is shallow at ~4-5 km depth and thus is well sampled by the diving-wave energy of this data set. Not surprisingly, we found that with this same data set, the performance of our approach dropped quickly when the depth of the salt body is very deep (e.g., ~10 km) and well beyond the penetration depth of diving waves. Therefore, for a typically deeper (e.g., >6 km) salt depth in the GoM, with possibly larger velocity errors, data sets with even longer offsets and lower frequencies are required.

Based on our experience applying our new FWI workflow to many different data sets, we think the vision of the future described by Michell et al. (2017) is likely correct: sparse OBN data with ultra-long offsets and a good low-frequency source may provide an economic yet adequate solution for automatic VMB using FWI in complex salt areas (Dellinger et al., 2016; Shen et al., 2018), with much less human interpretation than we have been practicing for the last two decades.

Acknowledgments

We thank CGG Multi-Client & New Ventures for permission to publish this work. We are grateful to numerous CGG colleagues, especially Jason Xu, Xin Hu, Bin Yu, Chang-Chun Lee, Jun Zhou, Chi Chen, and Xiao Huang, for successfully applying the workflow to different data sets. Special thanks go to BP for sharing their FWI success on Atlantis OBN data that inspired us.

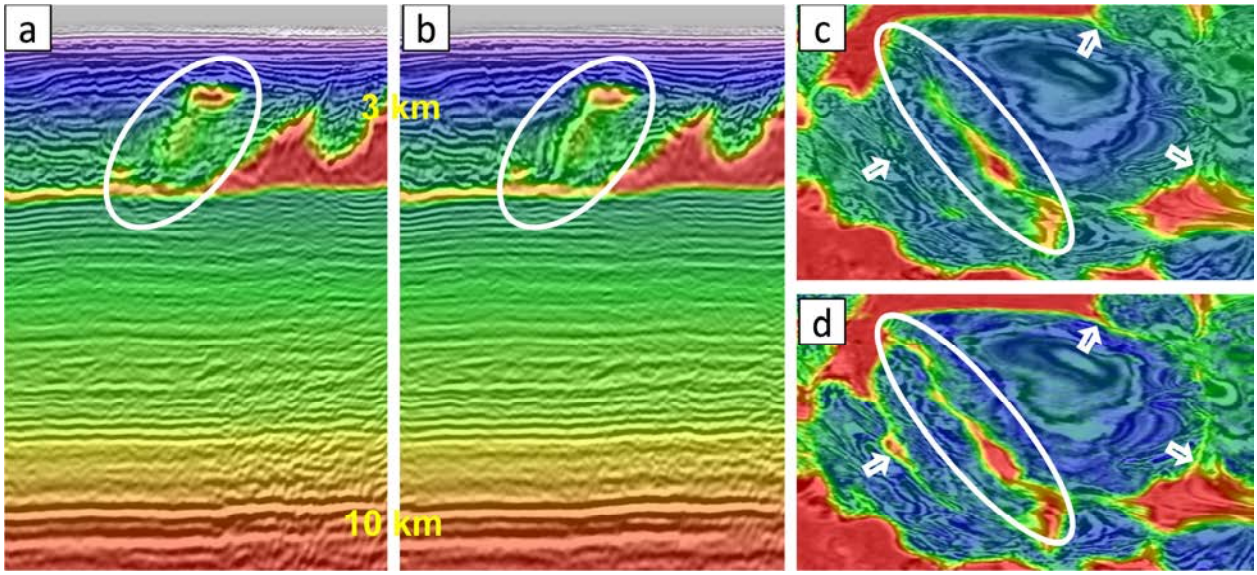

Figure 3: Inline section/depth slice at ~3 km with the velocity overlaid on RTM stack for (a)/(c) initial model and (b)/(d) straight output model from FWI. White circles and arrows mark where the salt bodies are appreciably updated by FWI.

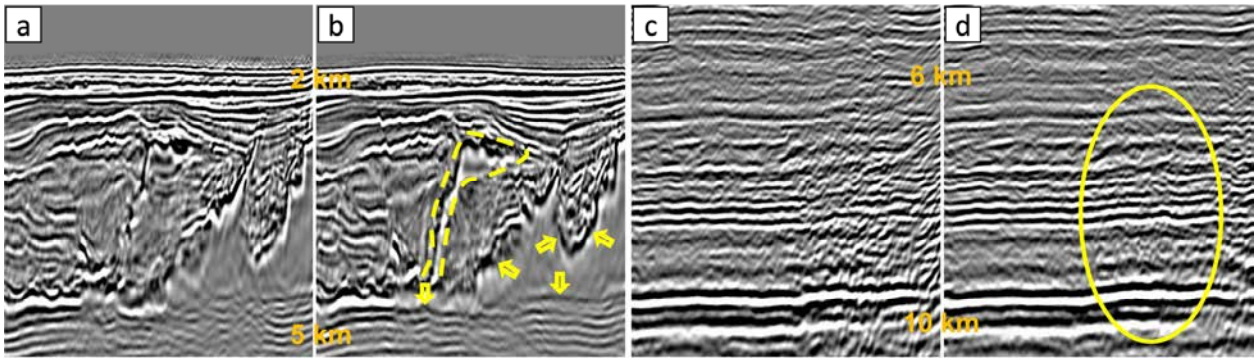

Figure 4: Inline section of RTM stack for (a)/(c) initial model and (b)/(d) straight output model from FWI at shallow/deep depth. The dashed yellow line marks a better defined small salt body after FWI and the yellow arrows mark the better imaged top-of-salt and base-of-salt. The yellow circle in (d) indicates the image improvement by FWI in the depth range from 7 km to 10 km.

10.1190/segam2018-2997711.1

REFERENCES

Dellinger, J., A. Ross, D. Meaux, A. Brenders, G. Gesoff, J. Etgen, J. Naranjo, G. Openshaw, and M. Harper, 2016, Wolfspar®, an" FWI-friendly" ultralow-frequency marine seismic source: 86th Annual International Meeting, SEG, Expanded Abstracts, 4891–4895, https://doi.org/10.1190/segam2016-13762702.1.

Lailly, P., 1983, The seismic inverse problem as a sequence of before stack migrations in Conference on inverse scattering: Theory and application, SIAM, 206–220.

Luo, Y., and G. T. Schuster, 1991, Wave-equation traveltime inversion: Geophysics, **56**, 645–653, https://doi.org/10.1190/1.1443081.

Ma, Y., and D. Hale, 2013, Wave-equation reflection traveltime inversion with dynamic warping and hybrid waveform inversion: 83rd Annual International Meeting, SEG, Expanded Abstracts, 871–876, https://doi.org/10.1190/segam2013-0087.1.

Mandroux, F., B. Ong, C. Ting, S. Mothi, T. Huang, and Y. Li, 2013, Broadband, long-offset, full-azimuth, staggered marine acquisition in the Gulf of Mexico: First Break, **31**, 125–132.

Michell, S., X. Shen, A. Brenders, J. Dellinger, I. Ahmed, and K. Fu, 2017, Automatic velocity model building with Complex salt: Can computers finally do an Interpreter's job?: 87th Annual International Meeting, SEG, Expanded Abstracts, 5250–5254, https://doi.org/10.1190/segam2017-17778443.1.

Shen, X., I. Ahmed, A. Brenders, J. Dellinger, J. Etgen, and S. Michell, 2017, Salt model building at Atlantis with full waveform inversion: 87th Annual International Meeting, SEG, Expanded Abstracts, 1507–1511, https://doi.org/10.1190/segam2017-17738630.1.

Shen, X., I. Ahmed, A. Brenders, J. Dellinger, J. Etgen, and S. Michell, 2018, Full-waveform inversion: The next leap forward in subsalt imaging: The Leading Edge, **37**, 67b1–67b6, https://doi.org/10.1190/tle37010067b1.1.

Tarantola, A., 1984, Inversion of seismic reflection data in the acoustic approximation: Geophysics, **49**, 1259–1266, https://doi.org/10.1190/1.1441754.

Warner, M., and L. Guasch, 2014, Adaptive waveform inversion: 84th Annual International Meeting, SEG, Expanded Abstracts, 1089–1093, https://doi.org/10.1190/geo2015-0387.1.